In-situ observation of martensitic transformation in an interstitial metastable high-entropy alloy during cathodic hydrogen charging

Dong Wang [a*], Xu Lu [a], Di Wan [a], Zhiming Li [b,c], Afrooz Barnoush [a]

[a] Department of Mechanical and Industrial Engineering, Norwegian University of Science and Technology, Richard Birkelands vei 2B, N-7491, Trondheim, Norway

[b] Max-Planck-Institut für Eisenforschung, Max-Planck-Str. 1, 40237 Düsseldorf, Germany

[c] School of Materials Science and Engineering, Central South University, Changsha 410083, China

[*] Corresponding author: Dong Wang
Email: dong.wang@ntnu.no
Address: Department of Mechanical and Industrial Engineering, Norwegian University of Science and Technology, Richard Birkelands vei 2B, N-7491 Trondheim, Norway

Abstract

We show for the first time that a critical amount of dissolved hydrogen can induce a phase transformation from γ-austenite to ε-martensite in an interstitial metastable high-entropy alloy. This is demonstrated by in-situ hydrogen charging in combination with nanoindentation and scanning probe microscopy, plus further electron channeling contrast imaging, X-ray diffraction, and transmission Kikuchi diffraction techniques. The transformed martensites appear as bands on the surface along γ-{111} habit planes, leading to an irreversible increase of hardness. The hydrogen-induced internal stress together with the intrinsic hydrogen effects are proposed to be responsible for the martensitic transformation upon hydrogen charging.

Keywords:

Hydrogen; High-entropy alloy; Martensitic transformation; In-situ electrochemical nanoindentation; Transmission Kikuchi diffraction

High-entropy alloys (HEAs) are a new class of alloys containing multiple principal elements, which provide a high mixing entropy and a massive solid solution state [1, 2]. Over the past decade, HEAs have attracted considerable attention owing to their excellent properties such as excellent combination of strength and ductility, outstanding fracture toughness, and good resistance to wear at both elevated and cryogenic temperatures [1-4]. These outstanding properties make HEAs as promising materials for applications in nuclear construction, liquid gas storage, transportation, and so forth [5]. However, a hydrogen-rich service environment can be deduced from the aforementioned applications, giving a high possibility of catastrophic and unpredictable failure known as hydrogen embrittlement. Up to now, most of the hydrogen embrittlement studies on HEAs are performed on the equiatomic CoCrFeMnNi alloy with the conclusion that this alloy has good resistance to hydrogen embrittlement at relatively low hydrogen concentration, while it still exhibits embrittlement phenomena when charged with high hydrogen content [6-8]. In addition, the hydrogen effect on a non-equiatomic dual-phase FeMnCoCr HEA

was investigated by Ichii et al. [9] via performing macroscopic tensile tests on pre-charged samples. The results showed reduction on both elongation and strength with obvious ε-martensite transformation, which was a combined effect from both hydrogen and deformation.

Recently, the interstitial metastable non-equiatomic HEAs have been developed exhibiting enhanced strength and strain hardening rate while maintaining good ductility compared to the equiatomic HEAs and the non-equiatomic HEAs without interstitial alloying [4, 10, 11]. This is due to the fact that this alloy design strategy can not only activate interstitial solid solution strengthening, but also tune phase stability and stacking fault energy (SFE) to achieve joint activation of transformation-induced plasticity (TRIP) and twinning-induced plasticity (TWIP) effects during deformation [12]. In such type of interstitial metastable HEAs, the TRIP effect suggests a deformation-induced phase transformation from face-centered cubic (FCC) γ phase to hexagonal close packed (HCP) ε phase [3, 11, 13]. To date, neither a hydrogen-related study at microscale nor the effect of hydrogen alone on the microstructure and nanomechanical properties of interstitial metastable HEAs has been discussed. In this study, we performed in-situ electrochemical hydrogen charging in combination with scanning probe microscopy (SPM) and nanoindentation. By this method combining with subsequent advanced characterization techniques, the effect of hydrogen alone on the microstructure and nanomechanical properties can be examined and understood.

The nominal chemical composition of the studied HEA is Fe-30Mn-10Co-10Cr-0.5C (at. %). The alloy ingot was cast in a vacuum induction furnace, hot-rolled at 900 °C, homogenized at 1200 °C for 2 h, and followed by water quenching. The alloy sample was further machined into discs with a thickness of 1.2 mm and a diameter of 12 mm. The disc samples were sequentially ground and polished till 1 μm diamond paste followed by electropolishing in a methanol/H_2SO_4 solution at 25 V for 80 s. After the surface preparation, a high-resolution scanning electron microscope (SEM, Quanta 650 FEG, Thermo Fisher Scientific Inc.) with a backscattered electron (BSE) detector as well as the electron backscatter diffraction (EBSD) techniques was used to study the original microstructure. After that, the sample was installed into an electrochemical cell consisting of a platinum counter electrode and a $Hg/HgSO_4$ reference electrode. Hereafter, all potentials in this study are reported versus this reference electrode. The electrochemical hydrogen charging was performed in a glycerol-based electrolyte, which consisted of 1.4 mol/L borax in glycerol and diluted with 20% distilled water to ensure the conductivity. In addition, 0.002 M $Na_2S_2O_3$ was added to promote the hydrogen absorption and prevent the hydrogen recombination [14]. This electrolyte has been proven to be reliable in keeping the sample surface from corrosion or oxidation due to its extremely low solubility and diffusivity of oxygen [15, 16]. The setup was further installed into a Hysitron Tribo-indenter TI950 equipped with a specially designed long-shaft Berkovich diamond tip, which was used for both SPM and nanoindentation test. In this study, the sample was firstly tested in air as the reference condition, followed by the same tests with in-situ hydrogen charging at -1400 and -1800 mV (the current densities were 0.12 and 0.85 mA/cm^2, respectively). After each cathodic charging, an anodic discharging at 0 mV was performed to check the reversibility after the desorption of hydrogen. Both cathodic charging and anodic discharging processes were applied at room temperature for more than 1.5 h till a stable hardness was reached. The SPM images were scanned on a same area and the hardness values were measured on the same grain at every 15 min. After the in-situ test, electron channeling contrast imaging (ECCI) was applied to characterize the deformed surface microstructure with 30 kV acceleration voltage and ~6.5 mm working distance; EBSD and grazing incidence X-ray diffraction (GIXRD, D8 DaVinci with LynxEye™ Superspeed detector) were performed to determine the phase distribution. The GIXRD was operated by using Cu Kα radiation (40 kV, 40 mA) at 0.75° incident angle at a step size of 0.02° and a counting time of 4.8 s per step; Transmission Kikuchi diffraction (TKD) was used to correlate the hydrogen effect on phase transformation with the dissolved hydrogen concentration

determined by thermal desorption spectroscopy (TDS) test. The TDS test was carried out by Bruker G4 PHOENIX with a mass spectrometer detector from 25 °C to 700 °C at a heating rate of 25 °C/min.

Fig. 1 shows the representative SPM images and the corresponding root-mean-square roughness R_q at different in-situ polarization conditions. The topography of sample surface in air condition before hydrogen charging is shown in Fig. 1a for reference. The original sample has a smooth surface with a R_q value of 0.056 nm as shown in Fig. 1g. The exact same position was continuously scanned in the following polarization conditions. Fig. 1b was captured after 2 h cathodic hydrogen charging at -1400 mV followed by 1.5 h anodic hydrogen discharging at 0 mV, and no noticeable change can be detected. Moreover, the R_q value was kept constant through the first sequence of hydrogen ingression and egression. However, the evolution of topography was detected when switched to -1800 mV cathodic polarization. As shown in Fig. 1c-e, the straight bands appeared after 1 h charging at -1800 mV, and these bands accumulated and became more noticeable by increasing the charging time. Fig. 1g shows that the roughness increased 32 times from 0.056 nm to 1.8 nm after 3.5 h charging at -1800 mV. After -1800 mV cathodic charging, the second anodic discharging was applied for a long time (13 h), and no irreversible phenomena were observed on both the SPM image and R_q value. Worthy of note, the accuracy of R_q values calculated from SPM images can be affected by factors such as tip bluntness, scan rate, and contact condition especially for in-situ condition and might not precisely reflect the actual surface roughness. Nevertheless, the change in the R_q values can be used as an indicator to reflect the trend of the actual surface roughness and martensitic transformation during in-situ hydrogen charging.

Fig. 1. (a-f) The representative SPM images during in-situ hydrogen charging/discharging under different conditions. The times marked on the top are the total polarization time and the times marked in the parenthesis below are the individual cathodic charging and anodic discharging times. g) The evolution of root-mean-square roughness R_q (nm) during in-situ hydrogen charging. The black arrows indicate the conditions shown in SPM images.

The nanoindentation test was performed on the same grain after each SPM scan, and the representative load-displacement curves are shown in the supplementary Fig.1. The hardness values were further calculated by using the Oliver-Pharr method [17]. As shown in Fig. 2, the original hardness in air was 3.63 GPa, and it accumulatively increased to a stable value of 4.07 GPa after 2 h cathodic charging at -1400 mV and then recovered to a similar value as in air condition after 1.5 h anodic discharging. By applying a higher charging potential at -1800 mV, a continuously increased hardness value was detected till a stable value was reached after 3.5 h charging, which showed a more significant hardness increment to 7.75 GPa. Moreover, a sudden hardness increment was observed in this cathodic charging condition after 2.25 h, which matches the apparent topography change (Fig. 1d). However, in comparison with the fully recovered hardness in the first anodic process, the hardness in the second anodic discharging condition showed only partial recovery (38.3%).

Fig. 2. The hardness values of the studied alloy under sequential polarization conditions. The black arrows indicate the conditions corresponding to the SPM images shown Fig. 1.

The reversible hardness increment during the first sequence of hydrogen ingression and egression was caused by the enhanced retarding stress on dislocation motion due to the increased lattice friction between dislocations and dissolved hydrogen [18]. The remained hardness increment as well as the topography change in the second sequence of charging and discharging was proposed due to hydrogen-induced phase transformation from γ-austenite to ε-martensite, which generally shows a very high hardness value [19]. In order to validate this assumption, further advanced characterization techniques were applied. Fig. 3a-3d show the ECC images of sample surface before (Fig. 3a) and after (Fig. 3b-3d) the in-situ test. The sample surface before charging contains uniformly distributed dislocations at a relatively low density. After the whole charging/discharging process, the deformation bands along three different directions are clearly visible. The orientations of these deformation bands, marked as black lines, are parallel to {111} slip traces indicated by red lines. Fig. 3d shows the ECC image at a higher magnification: the thin bands are stacking faults (SFs) and the thick bands are martensite plates forming through the overlapping of SFs [3]. The martensitic transformation can also be confirmed by GIXRD and EBSD analysis. Fig. 3e and 3f show the phase maps with the corresponding GIXRD spectra before and after hydrogen charging, respectively. It shows a pure γ-austenite phase in the original sample, and the parallel pattern consisting of ε-martensite lamellae can be observed within the γ grains after the whole in-situ hydrogen charging/discharging process. The γ-{111} and ε-{0001} pole figures constructed from the marked grains (1 to 4 in Fig. 3f) are shown as Fig. 3g and 3h, respectively. The poles are colored uniquely and encircled by unique shapes for each γ grain. It can be seen that the {0001} poles of ε phase appeared roughly at the same place as the {111} poles of γ phase for each indexed grain. This suggests a $\{111\}_\gamma \parallel \{0001\}_\varepsilon$ orientation relationship, which is in good agreement with the habit planes of ε-martensite transformation [20, 21]. It is worth noting that in contrast to the transformed α' and ε phases in austenitic stainless steels [22, 23], the ε phase is the only detected product phase in the current alloy. This might be due to a relatively high stability of the ε phase in the studied material [24]. This agrees with the phase transformation investigations of this material after cold rolling and tensile testing [11, 25].

Fig. 3. The ECC images of the sample surface before (a) and after (b-d) in-situ polarization test. (c) and (d) are the magnified areas of (b). The phase maps with the corresponding GIXRD spectra before (e) and after (f) hydrogen charging. The γ-{111} (g) and ε-{0001} (h) pole figures of the marked grains in (f).

It has been claimed within the framework of the defactant theory that the dissolved hydrogen can act as defactants and reduce the SFE [26-28]. A reduced SFE can facilitate the formation of SFs, which can serve as the nucleation sites for martensitic transformation [29]. According to the Kajiwara model [30], when stress is applied, a dislocation loop with partial Burgers vector is generated two atomic layers away from the pre-existing SF and a four-atomic-layer nano-sized ε-martensite is therefore produced. This thin ε-martensite grows thicker by consecutive formation of such dislocation loops at every second layer. The further growth of the martensite plates is thus presented as surface reliefs referring to the topographical changes. In this study, the charged hydrogen facilitated the formation of SFs on {111} closed packed planes, which acted as the nucleation sites for martensitic transformation. This hypothesis matches perfectly with the ECCI and EBSD results in Fig. 3 showing that the martensite formation is along {111} habit planes. Moreover, it has been proven by both experiments [31, 32] and simulations [33, 34] that hydrogen charging can lead to the formation of superabundant vacancies. The hydrogen-induced vacancies can further reduce the phase stability, resulting in martensitic phase transformation in interstitial-substitutional alloys [35]. Therefore, the hydrogen-induced vacancies might also facilitate the observed phase transformation in the current study. However, not only the intrinsic hydrogen effect can

promote the martensitic transformation, the hydrogen-induced internal stress also facilitates the phase transformation. During charging at -1800 mV, a high hydrogen concentration in the surface area is reached, which causes lattice expansion and results in high compressive internal stress [36]. This high internal stress acts as the driving force for γ to ε transformation during the cathodic charging process in this study.

Fig. 4. The SEM images of the sample surface with a specially milled micro-pillar before (a) and after (b) hydrogen charging. The magnified images of micro-pillar surface (c) and sample matrix (d) after hydrogen charging. (e) The TKD phase map of surface area showing the depth of martensitic transformation. (f) Hydrogen concentration as a function of depth at the end of -1800 mV charging process.

In order to prove the necessary conditions of hydrogen-induced internal stress on the phase transformation, an isolated square-shaped micro-pillar with the size of 4×4×2 μm³ was milled by focused ion beam (FIB, Helios Dual Beam, Thermo Fisher Scientific Inc., USA) as shown in Fig. 4a. The milling process was performed by a pre-designed one-step-pattern to avoid Ga ion-induced FIB damage. Without constraints surrounding the free-standing pillar, the internal stress induced by hydrogen charging can be easily released. By repeating the same hydrogen charging/discharging process, the pillar shows a smooth surface without any observable changes (Fig. 4c), while uniformly distributed martensitic bands are exhibited along three directions in the nearby matrix surface regions (Fig. 4d). This observation shows that a critical internal stress is the prerequisite for the martensitic transformation in this study. In order to determine the threshold of hydrogen concentration for this critical internal stress, a TKD characterization was performed. The specimen for TKD was cut by using FIB from the tested sample surface (deposited with protective carbon layer) till a depth of 5 μm and then milled from both sides to a final thickness of approximately 100 nm. The TKD result in Fig. 4e clearly shows that the ε-martensite was transformed within a depth of approximately 2.5 μm. The hydrogen content was measured by TDS on one sample (diameter 11.55 mm, thickness 0.81 mm, weight 0.6358 g) charged with the same conditions till the end of -1800 mV polarization as well as on one uncharged sample (diameter 11.55 mm, thickness 0.92 mm, weight 0.7243 g). The hydrogen content of the uncharged sample was measured as zero, while 1.0814 wppm hydrogen was quantified on the charged sample. The measured hydrogen content contains both diffusible hydrogen and trapped hydrogen, which are not differentiated in the current study and are considered to contribute together to the phase transformation. The surface hydrogen concentration C_s during charging at -1800 mV can be estimated by [37]

$$C_s = \frac{\omega C_M}{4}\sqrt{\frac{\pi}{Dt}} \tag{1}$$

where ω is the sample thickness, C_M is the mean hydrogen concentration of the sample (1.0814 wppm), and D is the hydrogen diffusion coefficient chosen as 3.2×10^{-16} m²/s [7]. The related hydrogen concentration $C(x,t)$ at distance x and time t was calculated by using the Fick's law based "semi-infinite" model [38]:

$$\frac{C(x,t) - C_0}{C_s - C_0} = 1 - \mathrm{erf}\left(\frac{x}{\sqrt{4Dt}}\right) \tag{2}$$

where C_0 is the initial hydrogen concentration as zero. The concentration profile of hydrogen in the sample is shown in Fig. 4f. Based on the TDS and TKD results, the threshold of hydrogen concentration for ε-martensite transformation can be estimated as 69.3 wppm, which was caused by 3.5 h hydrogen charging at -1800 mV (0.85 mA/cm^2) at the depth of 2.5 μm. Note that both the hydrogen charging current density and the dissolved hydrogen content resulting in martensitic transformation in this study are much less than that has been applied in many other studies involving martensitic transformation in the pre-charged samples after tensile tests [9, 39]. The above results suggest that it is important to distinguish between the tensile deformation induced martensite and the pre-charged hydrogen induced martensite in the future hydrogen embrittlement studies.

In summary, the influence of hydrogen alone on the phase transformation was investigated for the first time in an interstitial metastable HEA through in-situ hydrogen charging together with nanoindentation and SPM tests, plus further characterization by ECCI, EBSD, GIXRD and TKD techniques. The results show that cathodic hydrogen charging with a critical charging current density can lead to γ-austenite to ε-martensite transformation along the {111} habit planes. The transformed martensites appear as bands on the sample surface, leading to an irreversible increase of hardness. The hydrogen-induced internal stress together with the intrinsic hydrogen effect on SFE reduction and superabundant vacancies formation are proposed as the reasons for the martensitic transformation during hydrogen charging. Accordingly, it is necessary to consider these effects in future studies on hydrogen embrittlement and the design of hydrogen-tolerant alloys.

Reference

[1] Y. Zhang, T.T. Zuo, Z. Tang, M.C. Gao, K.A. Dahmen, P.K. Liaw, Z.P. Lu, Prog. Mater. Sci. 61 (2014) 1-93.

[2] J.W. Yeh, S.K. Chen, J.Y. Gan, S.J. Lin, T.S. Chin, T.T. Shun, C.H. Tsau, S.Y. Chang, Metall. Mater. Trans. A 35a(8) (2004) 2533-2536.

[3] Z. Li, K.G. Pradeep, Y. Deng, D. Raabe, C.C. Tasan, Nature 534(7606) (2016) 227-30.

[4] Z.M. Li, C.C. Tasan, H. Springer, B. Gault, D. Raabe, Sci. Rep. 7 (2017) 40704.

[5] Y.F. Ye, Q. Wang, J. Lu, C.T. Liu, Y. Yang, Mater. Today 19(6) (2016) 349-362.

[6] H. Luo, Z. Li, D. Raabe, Sci. Rep. 7(1) (2017) 9892.

[7] Y. Zhao, D.-H. Lee, M.-Y. Seok, J.-A. Lee, M.P. Phaniraj, J.-Y. Suh, H.-Y. Ha, J.-Y. Kim, U. Ramamurty, J.-i. Jang, Scr. Mater. 135 (2017) 54-58.

[8] K.E. Nygren, K.M. Bertsch, S. Wang, H. Bei, A. Nagao, I.M. Robertson, Curr. Opin. Solid State Mater. Sci. 22(1) (2018) 1-7.

[9] K. Ichii, M. Koyama, C.C. Tasan, K. Tsuzaki, Scr. Mater. 150 (2018) 74-77.

[10] Z. Li, Acta Mater. 164 (2019) 400-412.

[11] M.M. Wang, Z.M. Li, D. Raabe, Acta Mater. 147 (2018) 236-246.

[12] Z.M. Li, D. Raabe, Jom 69(11) (2017) 2099-2106.

[13] M. Koyama, T. Eguchi, K. Ichii, C.C. Tasan, K. Tsuzaki, Procedia Struct. Inte. 13 (2018) 292-297.

[14] M. Kappes, G.S. Frankel, R. Thodla, M. Mueller, N. Sridhar, R.M. Carranza, Corrosion 68(11) (2012).

[15] X. Lu, Y. Ma, M. Zamanzade, Y. Deng, D. Wang, W. Bleck, W.W. Song, A. Barnoush, Int. J. Hydrog. Energy 44(36) (2019) 20545-20551.

[16] X. Lu, D. Wang, Z. Li, Y. Deng, A. Barnoush, Mater. Sci. Eng. A 762 (2019) 138114.

[17] W.C. Oliver, G.M. Pharr, J. Mater. Res. 19(1) (2004) 3-20.

[18] D. Wang, X. Lu, Y. Deng, X. Guo, A. Barnoush, Acta Mater. 166 (2019) 618-629.

[19] H. Zhang, Y.Z. He, Y. Pan, Scr. Mater. 69(4) (2013) 342-345.

[20] G. Stone, G. Thomas, Metall. Trans. 5(9) (1974) 2095-2102.

[21] Z.H. Guo, Y.H. Rong, S.P. Chen, T.Y. Hsu, Scr. Mater. 41(2) (1999) 153-158.

[22] A.P. Bentley, G.C. Smith, Metall. Mater. Trans. A 17(9) (1986) 1593-1600.

[23] X.-S. Yang, S. Sun, T.-Y. Zhang, Acta Mater. 95 (2015) 264-273.

[24] W.J. Lu, C.H. Liebscher, G. Dehm, D. Raabe, Z.M. Li, Adv. Mater. 30(44) (2018).

[25] J. Su, X.X. Wu, D. Raabe, Z.M. Li, Acta Mater. 167 (2019) 23-39.

[26] R. Kirchheim, Scr. Mater. 62(2) (2010) 67-70.

[27] M.Q. Chandler, M.F. Horstemeyer, M.I. Baskes, P.M. Gullett, G.J. Wagner, B. Jelinek, Acta Mater. 56(1) (2008) 95-104.

[28] P.J. Ferreira, I.M. Robertson, H.K. Birnbaum, Mater. Sci. Forum 207-209 (1996) 93-96.

[29] N. Bergeon, S. Kajiwara, T. Kikuchi, Acta Mater. 48(16) (2000) 4053-4064.

[30] S. Kajiwara, D.Z. Liu, T. Kikuchi, N. Shinya, J. Phys. IV 11(Pr8) (2001) 199-204.

[31] Y. Fukai, K. Mori, H. Shinomiya, J. Alloys Compd. 348(1-2) (2003) 105-109.

[32] Y. Fukai, Phys. Scr. T103 (2003) 11-14.

[33] K. Ohsawa, F. Nakamori, Y. Hatano, M. Yamaguchi, J. Nucl. Mater. 458 (2015) 187-197.

[34] A. Metsue, A. Oudriss, X. Feaugas, MRS Adv. 1(24) (2016) 1785-1790.

[35] V.N. Bugaev, V.G. Gavriljuk, Y.N. Petrov, A.V. Tarasenko, Int. J. Hydrog. Energy 22(2-3) (1997) 213-218.

[36] Q. Yang, L.J. Qiao, S. Chiovelli, J.L. Luo, Scr. Mater. 40(11) (1999) 1209-1214.

[37] A.E. Pontini, J.D. Hermida, Scr. Mater. 37(11) (1997) 1831-1837.

[38] V. Olden, C. Thaulow, R. Johnsen, Mater. Des. 29(10) (2008) 1934-1948.

[39] Y.S. Chun, J.S. Kim, K.T. Park, Y.K. Lee, C.S. Lee, Mater. Sci. Eng. A 533 (2012) 87-95.
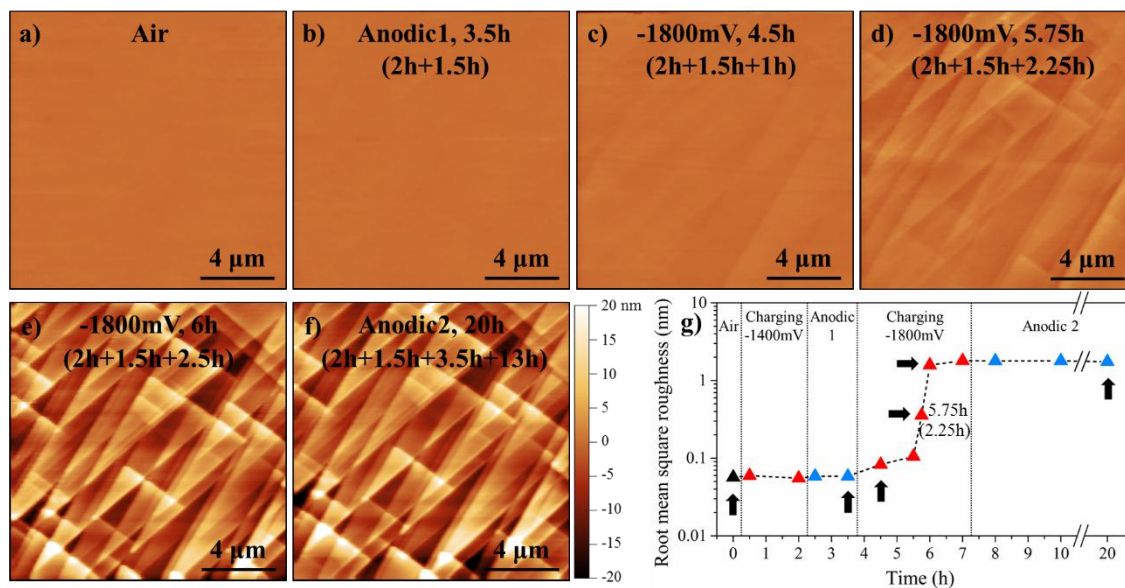
Fig. 1. (a-f) The representative SPM images during in-situ hydrogen charging/discharging under different conditions. The times marked on the top are the total polarization time and the times marked in the parenthesis below are the individual cathodic charging and anodic discharging times. g) The evolution of root-mean-square roughness R_q (nm) during in-situ hydrogen charging. The black arrows indicate the conditions shown in SPM images.
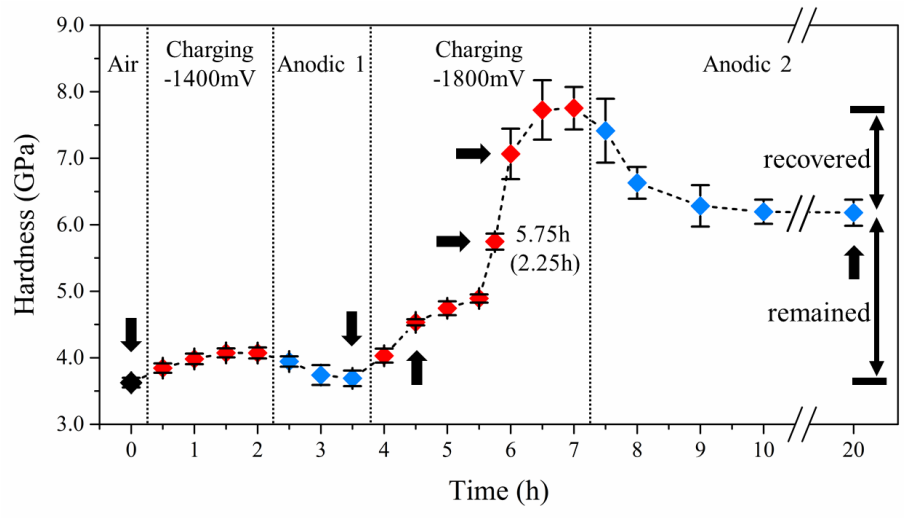
Fig. 2. The hardness values of the studied alloy under sequential polarization conditions. The black arrows indicate the conditions corresponding to the SPM images shown Fig. 1.
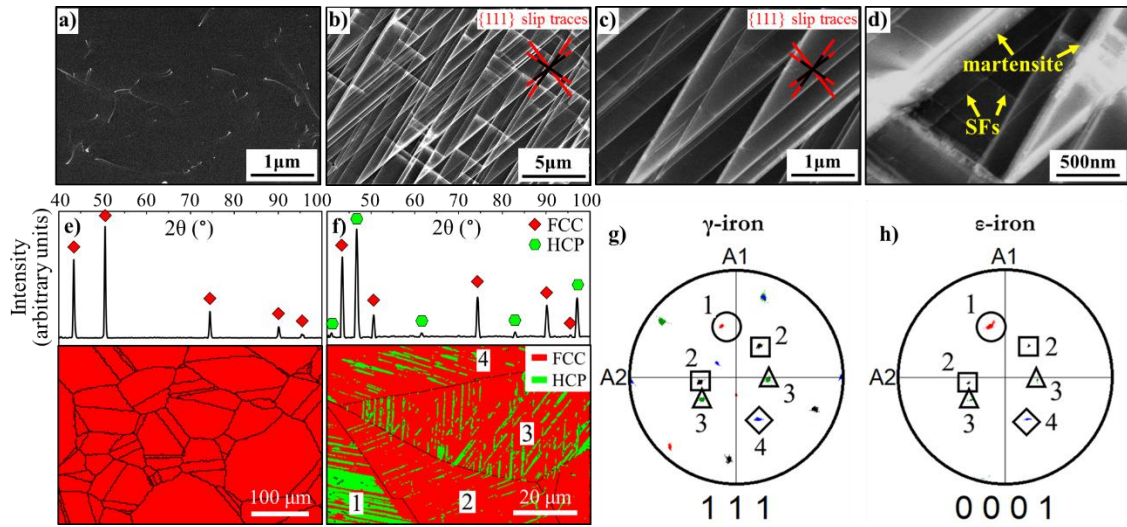
Fig. 3. The ECC images of the sample surface before (a) and after (b-d) in-situ polarization test. (c) and (d) are the magnified areas of (b). The phase maps with the corresponding GIXRD spectra before (e) and after (f) hydrogen charging. The γ-{111} (g) and ε-{0001} (h) pole figures of the marked grains in (f).
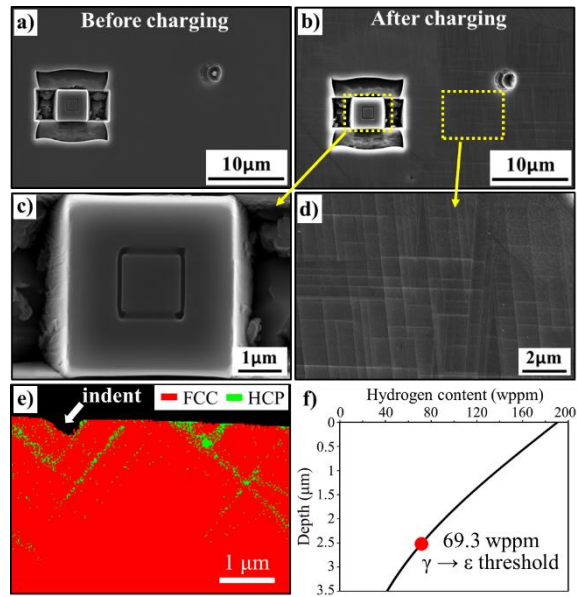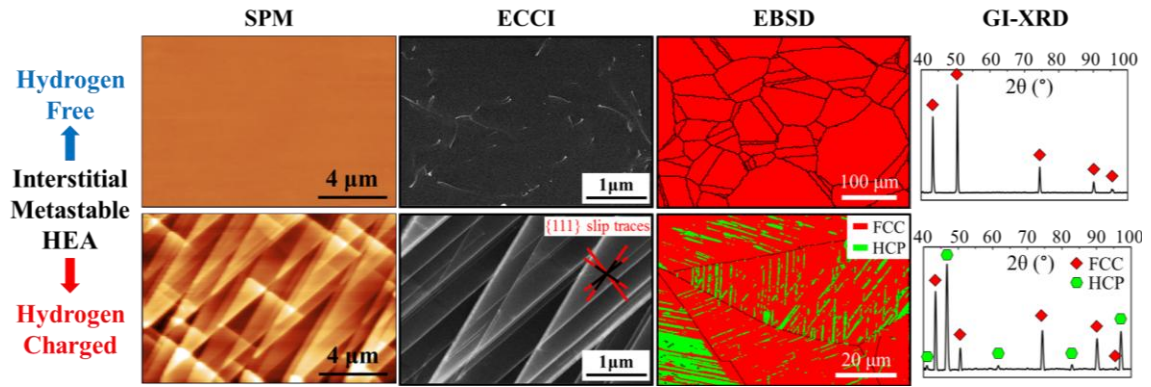
Fig. 4. The SEM images of the sample surface with a specially milled micro-pillar before (a) and after (b) hydrogen charging. The magnified images of micro-pillar surface (c) and sample matrix (d) after hydrogen charging. (e) The TKD phase map of surface area showing the depth of martensitic transformation. (f) Hydrogen concentration as a function of depth at the end of -1800 mV charging process.

Graphical Abstract

Supplementary Material